ISSN 0015-4628, Fluid Dynamics, 2026, Vol. 61:36. © Pleiades Publishing, Ltd., 2026.
Russian Text © The Author(s), 2025, published in Fiziko-Khimicheskaya Kinetika v Gazovoi Dinamike, 2025, Vol. 26, No. 7.

Modeling of Shocks and Vortex Zones in Supersonic Flow past a Body of Revolution at a High Angle of Attack

I. A. Shirokov[a,*] **and T. G. Elizarova**[b]

[a] *Moscow State University, Faculty of Computational Mathematics and Cybernetics, Moscow, Russia*

[b] *Keldysh Institute of Applied Mathematics, Moscow, Russia*

**e-mail: ivanshirokov@inbox.ru*

Received February 10, 2026; revised February 20, 2026; accepted February 20, 2026

Abstract—Direct numerical simulation of supersonic (Mach number is 1.5) viscous heat-conducting gas flow past a body of revolution (standard HB-2 model) at an angle of attack 29° is carried out. The calculation results make it possible to resolve the general structure of shocks around the body and obtain a good agreement of the stagnation parameters and the aerodynamic coefficients with theoretical and experimental data. The simulation was carried out on the basis of a quasi-gas dynamic (QGD) algorithm, that describes not only stationary and symmetric, but also non-stationary and asymmetric vortex zones that develop in flow. In this case, no additional turbulent viscosity is used in the calculations. It is shown that reducing the artificial dissipation coefficients in the QGD algorithm increases the accuracy of the modeling, bringing the calculated aerodynamic coefficients closer to the experimental data.

Keywords: quasi-gas dynamic algorithm, HB-2 model, supersonic flow, tetrahedral mesh

DOI: 10.1134/S001546282660447X

1. INTRODUCTION

The study of gas-dynamic flow past bodies of revolution is the topical problem in aerodynamics, since this shape is frequently used in practice. Vehicle control problems require studying the characteristics of subsonic and supersonic flows past such bodies, including those at high angles of attack. In this case, the flow configuration is complex three-dimensional, and for supersonic flows this is accompanied by the appearance of shock waves that affect the location of separation flow regions, the surface heat fluxes, and the aerodynamic forces exerted on the body. Such flows can be unsteady and asymmetric with appearance of turbulent zones and unstable asymmetric vortices. This can lead to generation of transverse forces, requiring additional investigations.

The primary methods for studying the described phenomena have been and remain wind tunnel tests of models. Theoretical studies of flow past bodies of revolution based on various empirical models and analogies are also widespread. With the development of computing technology, it has become possible to conduct three-dimensional modeling of flow past bodies of various shapes based on complete gas dynamics equations, which take into account most of the physical laws that manifest themselves in real flows [1]. However, such modeling is still a resource-intensive computational task and may require the use of various mathematical models that account for certain flow characteristics. In particular, flows with turbulent zones can be modeled using the large eddy simulation method (LES), which involves introducing appropriate variants of turbulent viscosity and applying highly accurate algorithms to solve the gas dynamics equations. Direct numerical simulation (DNS) has a more general scope of application, but is very expensive in terms of computing resources, since it is necessary to use large-size computational meshes, increase the computational time, use a large number of processors, etc.

One of the promising approaches for calculating the viscous heat-conducting gas flows past bodies of various shapes, taking into account the main physical phenomena that arise, is the quasi-gasdynamic (QGD) algorithm, which is similar to the DNS method, but is based on regularized Navier-Stokes equations, called the QGD equations [2–4]. The use of the QGD algorithm makes it possible to model both general flow patterns and possible unsteady phenomena (laminar-turbulent transition and vortex zones). Significant calculation experience has demonstrated the wide capabilities of the QGD algorithm in solv-

Fig. 1. Axisymmetric HB-2 model, general view.

ing the problems of modeling gas-dynamic flows in various configurations, in subsonic and supersonic variants, with or without turbulent zones [5–8].

In order to verify experimental and numerical methods for studying flows past axisymmetric bodies, in 1960 the standard HB-1 and HB-2 models [9] were proposed; the form of these models is typical for practical problems. A large number of data, obtained from wind tunnel tests of the HB-2 model [9–11] and from numerical simulations of flow past the model [1, 12, 13, 20] have been published. In the present paper, the QGD algorithm is applied to the problem of simulating supersonic (Mach number M = 1.5) viscous heat-conducting gas flow past the HB-2 model with the reference center body diameter $D = 0.1$ m and an angle of attack (AoA) equal to 29°. The obtained flow pattern is analyzed and compared with data available from literature, and the effect of artificial viscosity parameters on the calculation results is also analyzed.

2. FORMULATION OF THE PROBLEM

In [11], the results of experimental studies of supersonic air flow past HB-2 models in a wind tunnel at various Mach numbers and angles of attack were outlined. In the present paper, the formulation [11] is taken as a basis with the minimum Mach number M = 1.5 considered there and the maximum of the considered angles of attack 29°, while the Reynolds number $\mathrm{Re}_D = 2.3\times10^6$. In [9], the standard HB-2 model was described, and in Fig. 1 we have reproduced its general view.

In this paper, flow past the HB-2 model is calculated in the three-dimensional formulation in the Cartesian coordinates. An unstructured tetrahedral spatial mesh, constructed by means of the freely distributed Gmsh mesh generator [14], is used. It is known that the quality of the numerical solution of gas-dynamic problems is significantly determined by the quality of the mesh used. In [15], the effect of mesh characteristics on the results of modeling supersonic flow past the HB-2 model at zero angle of attack was studied. The questions of convergence of the results with mesh refinement were also investigated. The characteristics of the mesh used in the present study were selected taking into account the data obtained in [15], in which it was shown that the mesh with similar parameters is sufficiently good for modeling external supersonic flow at low Mach numbers. In this paper, the mesh construction technology is similar to that described in [15]. The mesh parameters are as follows: the number of cells is equal to 8986926, the characteristic sizes of cells are equal to 0.004 m on the model surface and 0.02 m on the outer surface of the computational domain.

In Fig. 2 we have reproduced the computational domain and the mesh in the cross-section $z = 0$, the direction of the free-stream flow (the model's axis of symmetry and the free-stream flow are located in the xy plane), as well as the inlet and outlet boundaries, are indicated.

Following [16], to estimate the quality of the mesh, we present the normalized (area under the curve is unity) distribution of the cell quality criterion $q = 3r/R$, where r is the radius of the sphere inscribed in the tetrahedron and R is the radius of the sphere circumscribed around the tetrahedron (Fig. 3).

In the case of a regular tetrahedron, $q = 1$; otherwise, $q < 1$. As q decreases, the tetrahedral cell "deteriorates" in terms of the accuracy of approximating the macroscopic equations. Figure 3 demonstrates fairly good overall quality of the mesh cells: most cells have $q > 0.6$. A detailed analysis of the distribution reveals that there are very few cells with $q < 0.3$ (around 10), and there are no cells with $q < 0.17$ at all.

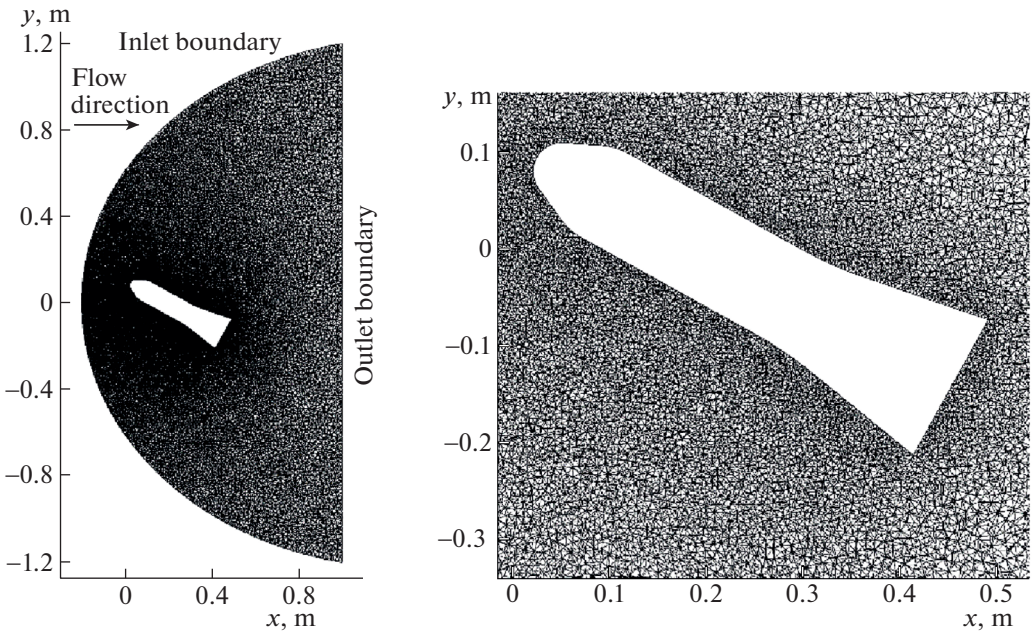

Fig. 2. Computational domain and tetrahedral mesh constructed by the Gmsh mesh generator in the cross-section $z = 0$, the general view on the left, a fragment on the right.

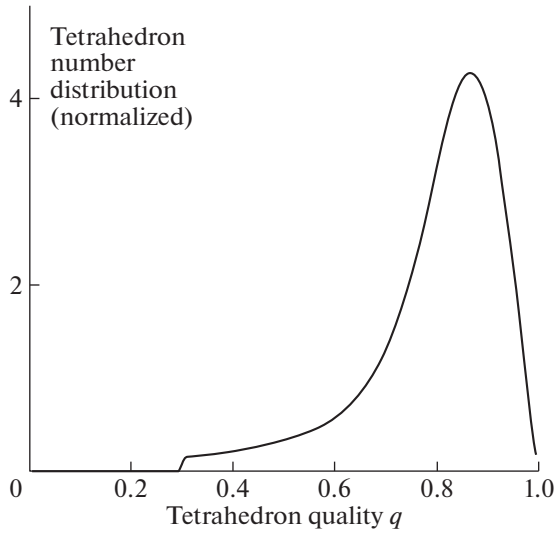

Fig. 3. Distribution of the quality criterion q of tetrahedral cells of the mesh used.

3. MODELING ALGORITHM

The QGD algorithm is based on the use of the following system of quasi-gasdynamic equations for an ideal polytropic gas [2–4]:

$$\frac{\partial}{\partial t}\rho + \nabla_i j_m^i = 0,$$

$$\frac{\partial}{\partial t}\rho u^j + \nabla_i \left(j_m^i u^j\right) + \nabla^j p = \nabla_i \Pi^{ij},$$

$$\frac{\partial}{\partial t} E + \nabla_i \left(j_m^i H\right) + \nabla_i q^i = \nabla_i \left(\Pi^{ij} u_j\right), \qquad (1)$$

where ρ is the density, u^i are the components of the macroscopic velocity, $p = \rho \mathrm{R} T$ is the pressure, T is the temperature, $E = \rho u^2/2 + p/(\gamma - 1)$ is the total energy per unit volume, and $H = (E + p)/\rho$ is the

total specific enthalpy. For air, the specific heat ratio is $\gamma = 1.4$. The expressions for the mass flux density vector j_m^i, the viscous stress tensor Π^{ij} and the heat flux q^i can be written as follows:

$$j_m^i = \rho\left(u^i - w^i\right), \quad w^i = (\tau/\rho)\left(\nabla_j \rho u^i u^j + \nabla^i p\right),$$

$$\Pi^{ij} = \Pi_{NS}^{ij} + \tau u^i \rho\left(u_k \nabla^k u^j + \left(\frac{1}{\rho}\right)\nabla^j p\right) + \tau\delta^{ij}\left(u_k \nabla^k p + \gamma p \nabla^k u_k\right),$$

$$\Pi_{NS}^{ij} = \mu\left(\nabla^i u^j + \nabla^j u^i - (2/3)\,\delta^{ij}\nabla^k u_k\right) + \zeta\delta^{ij}\nabla^k u_k,$$

$$q^i = q_{NS}^i - \tau u^i \rho\left(u_j \nabla^j \varepsilon + p u_j \nabla^j (1/\rho)\right), \quad q_{NS}^i = -\kappa\nabla^i T, \tag{2}$$

where $\varepsilon = p/(\rho(\gamma - 1))$ is the internal energy per unit mass of gas; Π_{NS}^{ij} and q_{NS}^i are the viscous stress tensor and the heat flux in the Navier–Stokes system; μ, ζ, and κ are the shear and bulk viscosity and thermal conductivity coefficients, respectively.

The shear viscosity coefficient μ is calculated using the temperature dependence

$$\mu = \mu_0 (T/T_0)^{\omega}, \tag{3}$$

where μ_0 is the shear viscosity of the gas at the free-stream flow temperature T_0 and $\omega = 0.74$ is the exponent of intermolecular interaction. The thermal conductivity coefficient is calculated as follows:

$$\kappa = \mu R\gamma/(\mathrm{Pr}(\gamma - 1)), \tag{4}$$

where the Prandtl number for air is $\mathrm{Pr} = 0.737$. The coefficient τ, which determines dissipation in the QGD algorithm, is defined as follows:

$$\tau = \mu/(p\mathrm{Sc}) + \alpha h/c, \tag{5}$$

the bulk viscosity coefficient is calculated using the formula

$$\varsigma = \mu((5/3) - \gamma) + \delta(h/c)\,p, \tag{6}$$

where h is the characteristic local size of the spatial cell, c is the local speed of sound, and $\mathrm{Sc} = 0.799$ is the Schmidt number for air.

Thus, the mathematical model used includes the following dissipative quantities: the shear viscosity coefficient μ (3) and the thermal conductivity coefficient κ (4), calculated based on the parameters of the real gas, as well as the bulk viscosity coefficient ς (6) and the coefficient τ (5). The latter regulates the magnitude of the QGD additives in formulas (2) and consists of two terms. The first is calculated based on the parameters of the real gas in terms of the shear viscosity coefficient and is of the order of the characteristic time between gas-particle collisions, while the second is artificial and can be adjusted using the coefficient α. In this problem, the Reynolds number is large, and the first term in (5) is much smaller than the second term throughout the computational domain. The coefficient τ ensures conditional stability of the algorithm and smooths out jumps and discontinuities in the solution according to the spatial mesh spacing. This is especially important for stabilizing the solution on shock wave fronts. To improve the accuracy of the solution, the coefficient α should be kept as small as possible. Typically, in calculations, it is set equal to 0.1–0.5 (in this paper, $\alpha = 0.5$ and 0.1).

However, in a number of problems, the stabilizing role of the τ-terms in describing shock waves turns out to be insufficient, so an additional adjustable artificial additive to the coefficient of bulk viscosity (6) is introduced into the algorithm. This coefficient also consists of two terms: the first is an approximation formula and is determined by the gas parameters, and the second is artificial term, which is adjusted using the numerical coefficient δ [5]. In this paper, δ takes the values 3 and 1. The first term in formula (6) is small compared to the second. Note that the τ-terms are small in the zone of large gradients in the boundary layer. The artificial additive to the bulk viscosity coefficient also disappears in the boundary layer, and thus the artificial additives do not distort the flow pattern near the model surface.

The numerical modeling technique is the same as that in [15]. We reduce the gas-dynamic parameters (density, velocity, pressure, temperature, energy) to dimensionless form. The characteristic length of 1 m and the density and the speed of sound in the free-stream flow are taken as dimensional parameters. Thus, in the free-stream flow $\rho = 1$, $p = 1/\gamma$, $T = 1$, and $U = \mathrm{M}$. In dimensionless variables, the equation of state takes the form $p = \rho T/\gamma$, in this case, the speed of sound $c = \sqrt{T}$ and the Reynolds number $\mathrm{Re}_D = \mathrm{M}D/\mu_0$.

Table 1. Variants of simulation

Variant	Value of the coefficient α (5)	Value of the coefficient δ (6)
1	0.5	3
2	0.5	1
3	0.1	1

The values of the gas-dynamic parameters are determined at mesh nodes; at points in the computational domain located between mesh nodes, the values of the gas-dynamic variables are determined as the arithmetic mean of the values at the nearest nodes. The finite-difference approximation of the macroscopic QGD equations is constructed using the control volume method; a barycentric control volume is constructed around each mesh node. Due to the non-uniformity of the spatial mesh, the algorithm has the first-order spatial approximation.

Initially, the free-stream parameters are specified on the inlet boundary (see Fig. 2). Within the computational domain, the same parameters are specified, except for the velocity: gas is stationary at the initial instant. The free-stream quantities are held constant on the inlet boundary. Soft conditions, allowing the gas to freely leave the domain, are imposed on the outlet boundary. No-slip conditions are imposed (the velocity vector is equal to zero) on the rigid boundary of the model; in this case, an additional boundary condition of the QGD algorithm is used: the normal derivative of the pressure is equal to zero. The model surface is assumed to be adiabatic.

We find the solution to the initial boundary value problem for mesh analogues of system (1)–(6) using a time-explicit finite-difference scheme that has first-order approximation in time. The time step is calculated as $h_t = \beta h/c$, where $\beta = 0.1$ is the Courant number, and h and c are the same local parameters as those in formulas (5)–(6). The calculations were performed using the K-100 hybrid supercomputer installed in the Supercomputer Center of Collective Usage of the Keldysh Institute of Applied Mathematics of the Russian Academy of Sciences [17]. Parallel computations based on the decomposition of the computational domain employing the MPI standard and the METIS library were used.

4. GENERAL FLOW PATTERN

The simulation is performed in three variants, which differ in the values of the artificial viscosity (Table 1). The effect of these coefficients on the calculation results will be discussed below.

Using the calculation experience [15], it was assumed that the flow pattern for each of the variants is formed over a dimensionless time equal to 10. To estimate the corresponding dimensional value, we take into account that in experiments [11], the source of air flow in the wind tunnel is a tank in which the gas is at rest at a temperature of 290 K. Applying the isentropic formula for the stagnation temperature [18, p. 108], we obtain that at M = 1.5 the free-stream flow temperature $T_0 = 200$ K. The speed of sound in the free-stream flow $c_0 = (\gamma R T_0)^{1/2} = 283$ m/s (we assume that the universal gas constant $R = 287$ J/(kg K)). Since the non-dimensionalization parameters were taken equal to 1 m and c_0, for the dimensionless time equal to 10 the dimensional time is 0.0353 s. During this time, a gas particle with velocity c_0 will travel 10 m (note that the model length is approximately 0.5 m, and the computational domain length is approximately 1.5 m). The number of steps in the difference scheme for dimensionless time 10 is approximately 10^5, and the computational time for a mesh with 8 986 926 cells when using 128 processor cores of the K-100 supercomputer is approximately 10 h.

In Fig. 4 we have reproduced the flow patterns: experimental data borrowed from [11] (Fig. 4a) and the simulation results for variants 1, 2, and 3 (Figs. 4b, 4c, and 4d, respectively). Figure 4a shows the schlieren images of the flow pattern obtained in experiment [11], corresponding to the density gradients (in fact, gradients of the refractive index) projected onto the plane of symmetry (the plane of figure). Positive values of the gradient along the flow are shown as dark areas, negative ones as light ones. High gradients (behind the rear region of the model) are not resolved in the schlieren image.

The calculation results (Figs. 4b–4d) are given in form of dimensionless density levels. A comparison of the experimental and calculated data reveals that the general shape of the shock waves is satisfactorily resolved in the simulation, the resolution in variants 2 and 3 (at lower values of artificial viscosity) being better than in variant 1. Two shock waves are clearly seen on the windward side of the model, as in the experiment. On the leeward side, two shock waves are also resolved in the simulation, while four shock

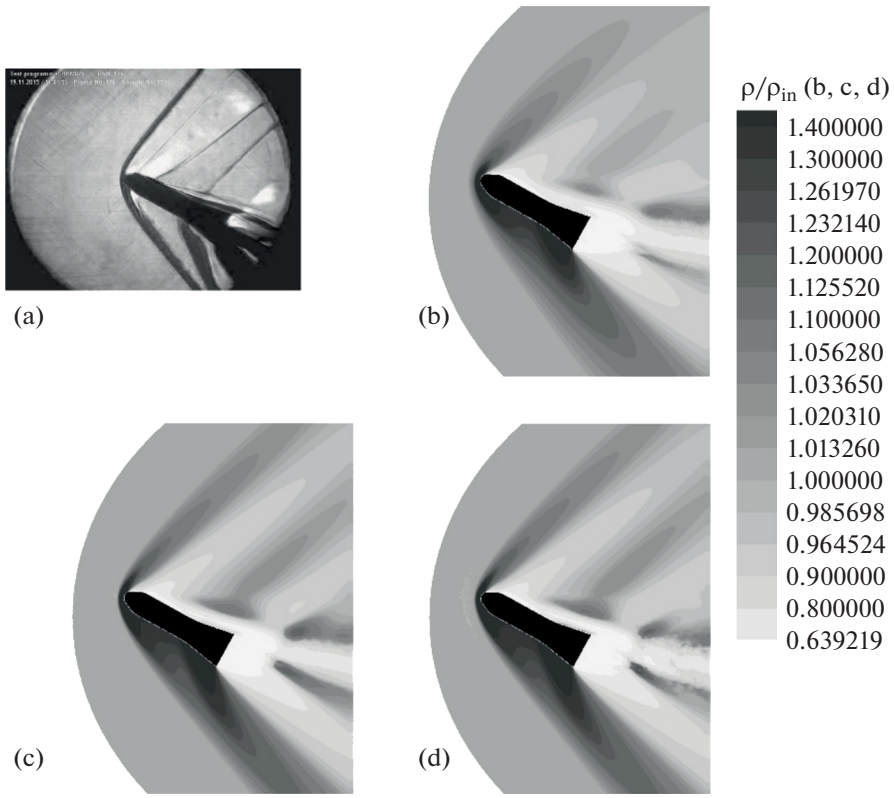

Fig. 4. Flow patterns in the cross-section $z = 0$: schlieren image in the experiment (a), density levels for simulation in variants 1–3 (b–d).

waves are observed experimentally (one of them is weak). Furthermore, the shock wave parallel to the model surface and located above the tail extension is relatively well resolved in the simulation. In the numerical calculation, the distance from this shock wave to the surface is somewhat greater than in the experiment.

Reducing the coefficient δ, which determines the artificial addition to the bulk viscosity (6), significantly improves the shock wave resolution, while reducing the coefficient α, which specifies an additional dissipation in the τ-terms of the QGD algorithm (5), has virtually no effect on the flow pattern at small δ. With further reductions in the artificial viscosity coefficients, the calculation loses stability.

In Fig. 5 we have reproduced levels of the dimensionless pressure and the Mach number for the simulation in variant 2. In addition to the shock waves visible at the density levels (Figs. 4b–4d), the pressure levels additionally show a weak wave with an increase in the pressure on the leeward side of the model ($x =$ 0.2 m, $y = 0.5$ m). This corresponds to the shock wave in this region observed experimentally (Fig. 4a).

The flow pattern obtained can be qualitatively compared with the results of simulations of flow past the HB-2 model at M = 3 and the angle of attack 8° obtained in [1, pp. 47–48]: regions of increase in the local Mach number (exceeding the freestream Mach number) are observed in areas roughly corresponding to the pressure drop regions on the leeward side of the model and behind the rear region. These regions have a similar structure in [1] and in the present paper. The pressure distribution pattern is also qualitatively similar to the pattern of flow past the HB-2 model obtained in [13] in calculations at M = 3 and the angle of attack equal to 16º.

5. VORTEX ZONES AND FLOW UNSTEADINESS

In Figs. 6–8 we have reproduced the calculated density levels and streamlines at various time instants: the formed flow pattern is shown to the left and on the right the calculation is continued at the dimensionless time 3.9 (0.014 s) in the cross-sections $z = 0$ (Fig. 6), $x = 0.414228$ m (Fig. 7), and $x = 0.491801$ m (Fig. 8). The simulation was carried out in variant 2 (see Table 1). We took the last two cross-sections (Figs. 7 and 8) so that they touch the rear boundary.

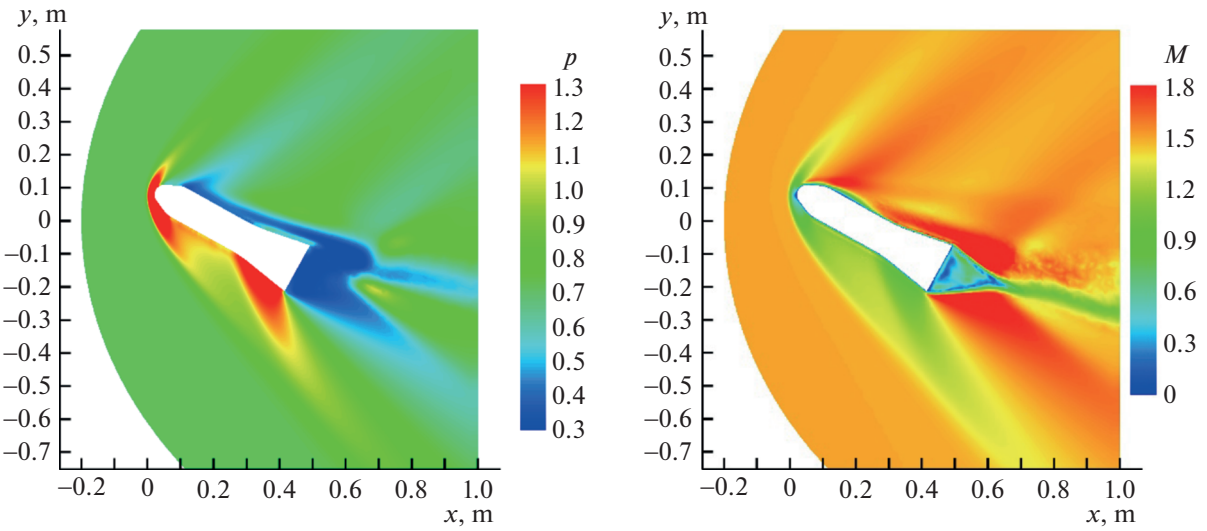

Fig. 5. Pressure levels (on the left) and Mach number levels (on the right) in the cross-section $z = 0$, simulation (variant 2).

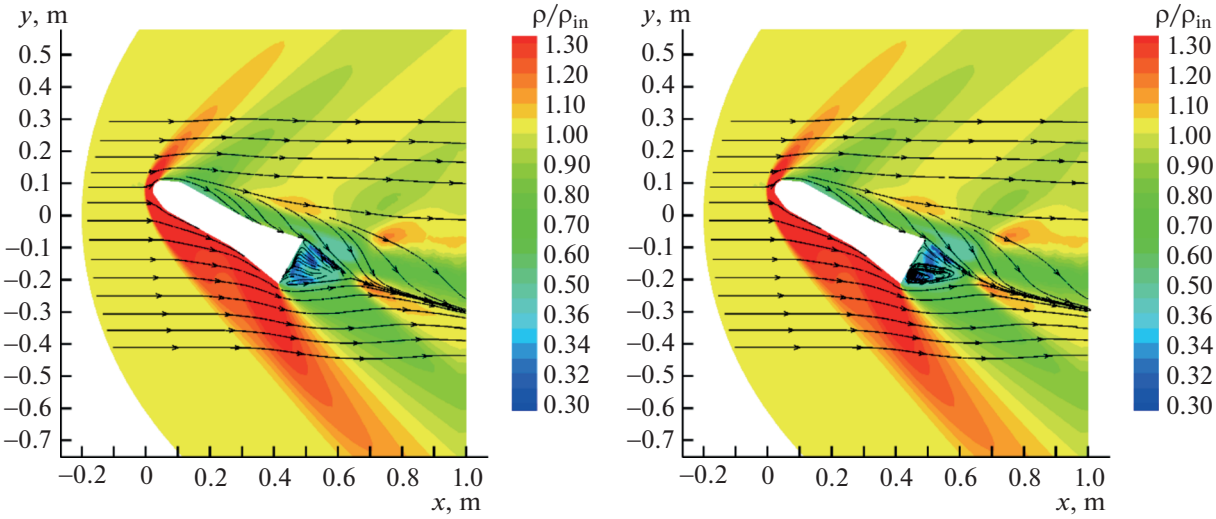

Fig. 6. Density levels and streamlines at time instants that differ by 0.014 s in the cross-section $z = 0$, simulation (variant 2).

In three cross-sections shown in Figs. 6–8, the density levels and the streamlines are steady-state everywhere except for the region behind the model's rear cross-section, where an unsteady vortex zone, visible in Figs. 6 and 8, forms. In Fig. 7, we can see two stationary vortices, that form on the leeward side of the cylindrical part of the model. Since the cross-section shown in Fig. 7 does not intersect the vortex zone, in this figure the density levels and streamlines are steady-state.

In Fig. 8 we have reproduced the cross-section through the vortex zone behind the rear region. It is clearly seen that in this zone the vortex and density level patterns differ significantly at different instants. Furthermore, we can see asymmetry in both the vortices and the density distribution. This asymmetry can lead to the appearance of a transverse force, whose study is an important problem in the aerodynamics of flow past bodies of revolution [19]. The location of the zones of minimum density approximately corresponds to the centers of the vortices.

Thus, the flow simulation shows the formation of two steady-state vortices on the leeward side and an unsteady vortex pattern behind the rear region, the flow pattern being essentially three-dimensional.

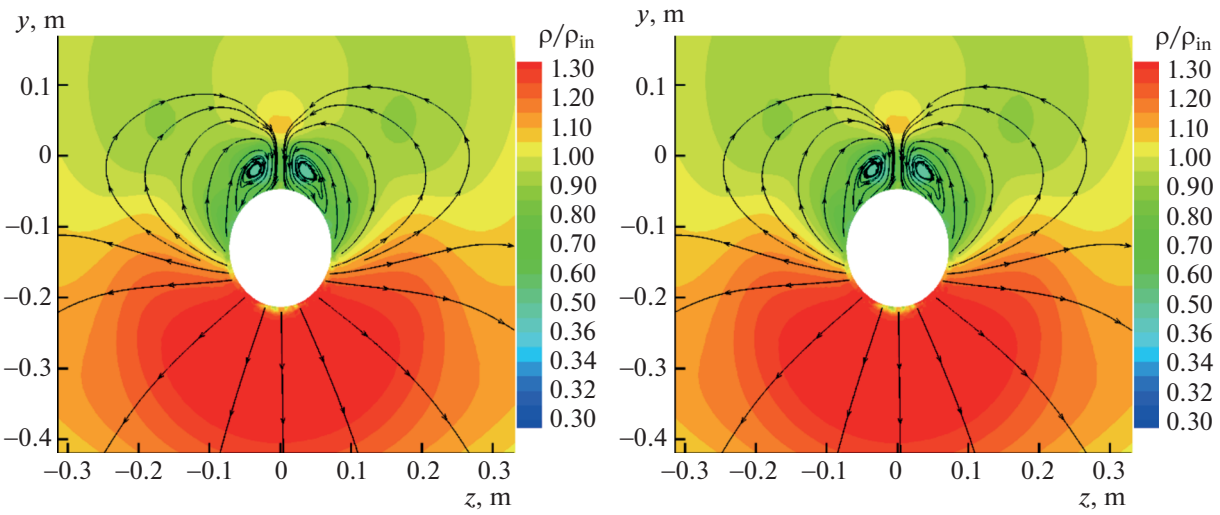

Fig. 7. Density levels and streamlines at time instants that differ by 0.014 s in the cross-section $x = 0.414228$ m, simulation (variant 2).

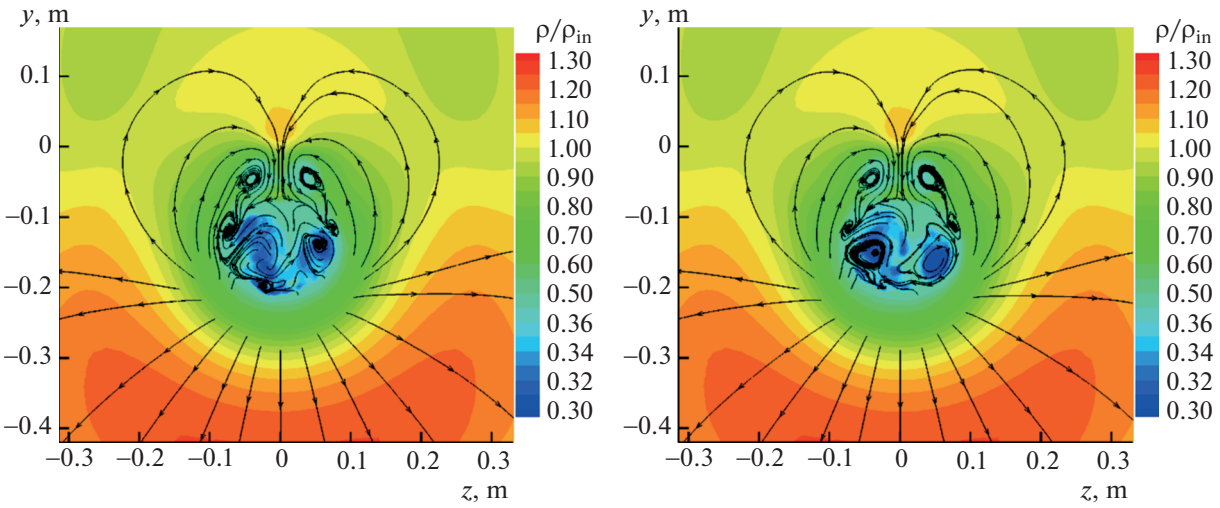

Fig. 8. Density levels and streamlines at time instants that differ by 0.014 s in the cross-section $x = 0.491801$ m, simulation (variant 2).

A similar structure of steady-state vortices on the leeward side was found in [13] in simulations of flow past the HB-2 model at M = 3 and the angle of attack equal to 16°.

To illustrate the spatial flow structure, in Fig. 9 we have reproduced the streamlines in the neighborhood of the model from two perspectives. It can be seen that the flow in the leeward vortices has a spiral nature.

6. STAGNATION PARAMETERS AND AERODYNAMIC COEFFICIENTS

In Fig. 10 (to the left) we have compared the dimensionless values of the stagnation parameters obtained in the simulation (symbols) and the theoretical data (horizontal lines). The stagnation parameters were taken on the surface of the body nose at the point at which the density reaches maximum. The theoretical data were calculated from the Rankine–Hugoniot conditions and isentropic formulas [18, p. 108] and [3, p. 130] under the assumption that the flow stops completely at the point of maximum density near the surface. The numbers of variants on the abscissa axis correspond to Table 1. It can be seen that the simulation results in variants 2 and 3 are closer to the theoretical ones than in variant 1. A com-

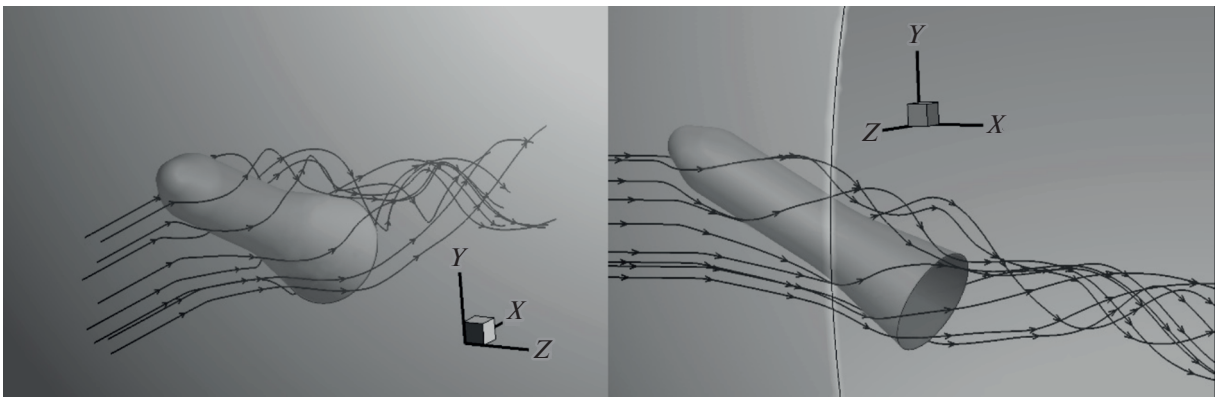

Fig. 9. Spatial streamlines, simulation (variant 2).

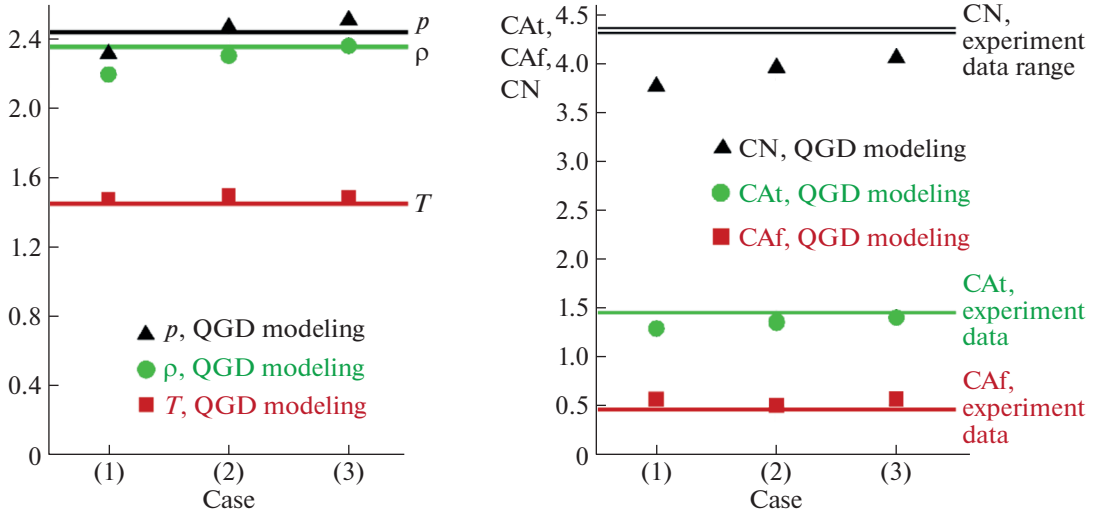

Fig. 10. Dimensionless stagnation parameters, simulation and theory (on the left). Aerodynamic coefficients, simulation and experiment (on the right).

parison of the results in variants 2 and 3 shows the effect of decrease in the coefficient α (5). Thus, the stagnation parameters obtained in the simulation with the small artificial viscosity coincide fairly well with their theoretical values.

In Fig. 10 (to the right) we have compared the aerodynamic coefficients of the total axial force *CAt*, the forebody axial force *CAf* , and the normal force *CN* obtained in simulation with the experimental values from [11]. The calculation results are shown by symbols, and the experimental data are shown by horizontal lines. The total axial force is calculated in post-processing of the simulation data as the projection of the total aerodynamic force (calculated using the pressure integral over the surface) onto the axis of symmetry of the model. Similarly, the normal force is the projection of the total aerodynamic force onto a line perpendicular to the plane of symmetry of the model and lying in the *xy* plane.

The axial forebody force is a component of the total axial force when calculating the aerodynamic impact on the model surface without taking into account the rear region, while it is assumed that the base is subject to a constant pressure equal to the static pressure in the free-stream flow. To calculate the aerodynamic coefficients, the forces considered above are normalized to the free-stream dynamic pressure $\rho_0 u_0^2 S_0/2$, where, in dimensionless form, we have $\rho_0 = 1$ and $u_0 = M$. The reference area $S_0 = (\pi/4) D^2 = 0.00785$ m^2 [9].

It can be seen that, with decrease in the artificial viscosity (coefficients α and δ), the calculation results become closer to the experimental data. The values of *CAt* and *CAf* obtained in variants 2 and 3 are in good

agreement with the experiment, the value of *CN* is somewhat underestimated. Note that in experiments [11], the model is fixed on a support (a cylindrical rod coaxial with the model), and the support diameter is greater than the value recommended in [9]. In the experiments, an increase in the support diameter was required to increase the structural strength for testing at high angles of attack. It is reasonable to assume that the underestimation of *CN* in the simulation is due to the effect of a large-diameter support in the experiment at a high angle of attack (obviously, with increase in the angle of attack, the effect of the support on *CN* also increases). Note that the values of *CN* obtained experimentally [11] have a small spread. This is reflected in Fig. 10 on the right. The flow unsteadiness in the simulation, which is illustrated by Figs. 6 and 8, results in the aerodynamic coefficients varying with time (by about 1–2%). These changes are not shown in Fig. 10 on the right. No effect of flow unsteadiness on the stagnation parameters was detected.

5. SUMMARY

Numerical simulation of supersonic flow past an HB-2 body of revolution at large angle of attack using the QGD algorithm on Gmsh tetrahedral meshes makes it possible to satisfactory resolve the general structure of the shock waves around the body, as well as to obtain a good agreement of the stagnation parameters and aerodynamic coefficients to the theoretical and experimental data. Furthermore, the simulation performed reveals the formation of two stationary vortices formed on the leeward side of the cylindrical part of the body, as well as a zone of unsteady vortices behind the base region. Reducing the values of the artificial viscosity coefficients in the QGD algorithm (Table 1) increases the accuracy of the simulation.

The experience with numerical simulation shows that the QGD algorithm performs well on unsteady-state problems and describes well the occurrence of unsteady and asymmetric flows, without requiring the introduction of an additional turbulent viscosity into the mathematical model. Application of the QGD algorithm to the problem presented here demonstrates that unsteadiness does indeed occur, but only in a limited region near the rear part of the body and has virtually no effect on the flow characteristics in the rest of the region. Therefore, problems of this type can be modeled using simpler numerical algorithms focused on finding steady-state solutions. The latter significantly simplifies the numerical calculation, but, in principle, can lead to the fact that effects caused by the asymmetric flow pattern not being taken into account.

In [6], the problem of calculating supersonic flow at an angle of attack of an axisymmetric model with a tail extension, similar to the problem considered in the present paper, was investigated. In both works, the calculations are performed based on the QGD algorithm using a similar methodology. In [6], relatively good correspondence between the pressure distribution over the surface and the vortex pattern of the flow and the experimental data was obtained. This work complements study [6] in terms of confirming the applicability of the QGD algorithm to calculating supersonic flow past bodies of revolution at various angles of attack and the correspondence of the modeling results to various experimental data. Paper [20] on a closely related topic was recently published. This confirms the interest in studying the flow past axisymmetric bodies at large angles of attack. The data obtained in the present work are generally consistent with the calculation results presented in [20].

FUNDING

The article was funded by the state assignment of Moscow State University, the topic no. 126021717441-4. No additional grants were obtained to carry out or direct this study.

CONFLICT OF INTEREST

The authors of this work declare that they have no conflicts of interest.

References

1. Surzhikov, S. T., Numerical interpretation of experimental data on aerodynamics of the HB-2 model using computer codes USTFEN and PERAT-3D, *Physical-Chemical Kinetics in Gas Dynamics*, 2020, vol. 21, no. 1. https://doi.org/10.33257/PhChGD.21.1.900
2. Chetverushkin, B.N., *Kinetic Schemes and Quasi-Gas Dynamic System of Equations*, Barselona: CIMNE, 2008.
3. Elizarova, T.G., *Quasi-Gas Dynamic Equations*, Dordrecht: Springer, 2009. https://doi.org/10.1007/978-3-642-00292-2

4. Sheretov, Yu.V., *Regulyarizovannye uravneniya gidrodinamiki* (Regularized Hydrodynamic Equations), Tver: Tver State University, 2016.

5. Elizarova, T. G. and Shirokov, I.A., Artificial dissipation coefficients in regularized equations of supersonic aerodynamics, *Doklady Mathematics*, 2018, vol. 98, no. 3, pp. 648–651. https://doi.org/10.1134/S1064562418070141

6. Shirokov, I. A. and Elizarova, T. G., Computational experiment in the problem of supersonic flow around a blunt body with tail expansion, *Mathematical Models and Computer Simulations*, 2020, vol. 12, no. 3, pp. 433–444. https://doi.org/10.1134/S0234087919100095

7. Shirokov, I. A., *Numerical Study of the Aerodynamic Characteristics of a Triangular Wing at Different Angles of Attack and Large Mach Numbers*, Moscow: Keldysh Institute of Applied Mathematics of Russian Academy of Science, Preprint no. 56, 2021. Available at https://library.keldysh.ru/preprint.asp?id=2021-56

8. Shirokov, I. A. and Elizarova, T. G., Modeling of unsteady subsonic flow around an axisymmetric body with a turbulator, *Thermophysics and Aeromechanics*, 2022, vol. 29, no. 1, pp. 35–42. https://doi.org/10.1134/S0869864322010024

9. Gray J. D., *Summary Report on Aerodynamic Characteristics of Standard Models HB-1 and HB-2,* AEDC-TDR-64-137, 1964.

10. Ceresuela R., *Maquettes Etalons HB-1 et HB-2. Caracteristiques Aerodynamiques Mesurees dans les Souffleries de l'O.N.E.R.A. de Mach 2 a Mach 16.5*, Note Technique O.N.E.R.A., 1968, no. 123. 24 p.

11. Vukovic, Dj. and Damljanovic, D., HB-2 high-velocity correlation model at high angles of attack in supersonic wind tunnel tests, *Chinese Journal of Aeronautics*, 2019, vol. 32(7), pp. 1565–1576. https://doi.org/10.1016/J.CJA.2019.03.022

12. Kryuchkova, A. S., Numerical simulation of supersonic flows over ballistic models using UST3D programming code, *Physical-Chemical Kinetics in Gas Dynamic*, 2018, vol. 19, no. 4. https://doi.org/10.33257/PhChGD.19.4.783

13. Chetverushkin, B. N., Borisov, V. E., Davydov, A. A., Lutsky, A. E., and Khankhasaeva, Ya. V., Numerical simulation of heat flux around a ballistic model based on the hyperbolic quasi-gasdynamic system of equations, *Mathematical Models and Computer Simulations*, 2021, vol. 13, no. 5, pp. 844–852. https://doi.org/10.20948/mm-2021-02-03

14. *Gmsh: Three-Dimensional Finite Element Mesh Generator*. Available at https://gmsh.info

15. Shirokov, I. A. and Elizarova, T. G., Influence of tetrahedral mesh characteristics on the accuracy of supersonic flow modeling of axisymmetric model, *Physical-Chemical Kinetics in Gas Dynamics,* 2025, vol. 26, no. 1. https://doi.org/10.33257/PhChGD.26.1.1173

16. Ermakov, M. K. and Kryuchkova, A. S., Generation of unstructured tetrahedral meshes for flow past flight vehicles based on open packages, *Physical-Chemical Kinetics in Gas Dynamic*, 2020, vol. 21, no. 2. https://doi.org/10.33257/PhChGD.21.2.897

17. K-100 System, Keldysh Institute of Applied Mathematics RAS, Moscow. Available at https://www.kiam.ru/MVS/resourses/k100.html

18. Loitsianskii, L.G., *Mechanics of Liquids and Gases*, New York: Pergamon Press, 1966.

19. Gumerov, A. V., Gumerova, L. V., and Balzannikova, Y. M., Analysis of transverse force in the case of flow about bodies of revolution at high angle of attack, *VESTNIK of Samara University. Aerospace and Mechanical Engineering*, 2009, vol. 8, no. 1, pp. 14–23 [in Russian]. https://doi.org/10.18287/2541-7533-2009-0-1(17)-14-23

20. Yatsukhno, D., Numerical study of the HB-2 standard model aerodynamics at the supersonic velocities, *Physical-Chemical Kinetics in Gas Dynamics*, 2024, vol. 25, no. 7. https://doi.org/10.33257/PhChGD.25.7.1172

Translated by E.A. Pushkar